Environmental Science & Technology

pubs.acs.org/est

Article

Spontaneous Abiotic Reduction of Arsenate to Arsenite Mediated by Structural Fe(II) Resulting from Abundant Oxygen Vacancy Clusters in Poorly Crystalline Ferrihydrite in Drought Environments

Yongjin Xiang, Jingtao Hou,* Lu Ren, Juan Xiong, Biao Wan, Mingxia Wang, Wenfeng Tan, and Andreas Kappler

Cite This: *Environ. Sci. Technol.* 2025, 59, 5191−5201

Read Online

ACCESS | Metrics & More | Article Recommendations | Supporting Information

ABSTRACT: The reduction of As(V) to As(III) has been proposed as an undesirable process, increasing the mobility and toxicity of arsenic. Although most studies revealed that As(V) reduction occurs in the aqueous phase, it remains unclear whether abiotic As(V) reduction driven by minerals in drought environments also exists. In this study, we examined the transformation of As(V) to As(III) mediated by ferrihydrite during drying processes using high-resolution X-ray photoelectron spectroscopy (XPS) and X-ray absorption near edge structure (XANES) spectroscopy analyses. The results revealed that nearly 40.8% of ferrihydrite-sorbed As(V) was transformed to As(III) after placing the As(V)-adsorbed ferrihydrite solids in a drought-tolerant environment for 7 days. As(V) reduction occurred under both oxic and anoxic conditions, with the reduction rate being higher in an anoxic atmosphere than in oxygen and air. Chemical analysis revealed the presence of structural Fe(II) in ferrihydrite, which was attributed to the abundance of oxygen vacancy clusters, as evidenced by positron annihilation lifetime (PAL) analysis. Fe L-edge XANES analysis and DFT calculations demonstrated that structural Fe(II) in dried ferrihydrite played a vital role in As(V) reduction, inducing electron transfer from Fe to As atoms. The findings of this study highlight a potentially important but long-overlooked As(V) reduction pathway at mineral surfaces under drought conditions in dried soils.

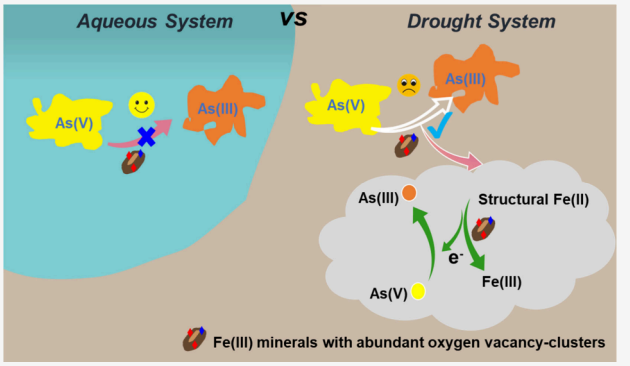

KEYWORDS: *Abiotic reduction, Arsenate, Iron (oxyhydr)oxide, Vacancy defects, Drought conditions*

Downloaded via UNIV TUEBINGEN on March 18, 2025 at 21:04:28 (UTC).
See https://pubs.acs.org/sharingguidelines for options on how to legitimately share published articles.

1. INTRODUCTION

Arsenic (As) is a metalloid commonly found in polluted soils that has extensively increased public concern, as it can enter the food chain through crop consumption in soil-plant systems, posing a serious threat to human health due to its high toxicity and carcinogenicity. The mobility and toxicity of As are strongly dependent on its redox state once it is released into the environment.[1] In natural environments, arsenate [As(V)] and arsenite [As(III)] are the two predominately inorganic arsenic species, with As(V) exhibiting lower mobility and toxicity than As(III).[2] The reductive transformation of As(V) to As(III) is therefore regarded as an adverse process that enhances arsenic mobilization, increasing the migration risk of As in natural environments.

In general, the biotic pathway triggered by microorganisms is considered the dominant pathway for As(V) reduction in soils and sediments.[3] For example, Cai et al. reported three anaerobic As(V)-reducing bacterial strains isolated from arsenic-contaminated soil, which were capable of rapidly reducing high As(V) concentrations (e.g., 60 mM) under anoxic conditions.[4] Guo et al. revealed that aerobic As-resistant bacteria isolated from a high-arsenic aquifer sediment possessed *arr* and *ars* genes, resulting in the reduction of dissolved As(V), goethite-adsorbed As(V), scorodite As(V), and sediment As(V) in the presence of organic carbon as the electron source.[5] Additionally, a significant level of As(III) was observed to be released from dissimilatory As(V) reduction of ferrous arsenate by *Shewanella* sp. strain ANA-3, which was explained by its extracellular reduction through *c*-type cytochromes originating from the cell wall.[6] Except for biotic processes, abiotic pathways are also observed to contribute to As(V) reduction but are often overlooked. For example, Perez et al. revealed the partial reduction of initial As(V) to As(III)

Received: October 15, 2024
Revised: February 21, 2025
Accepted: February 24, 2025
Published: March 5, 2025

© 2025 American Chemical Society

https://doi.org/10.1021/acs.est.4c10674
Environ. Sci. Technol. 2025, 59, 5191−5201

from mineral-bound As(V) in the presence of Fe^{2+} ions under aqueous anoxic conditions.[7] Jiang et al. found that dissolved humic acids showed different redox-active functional groups, enabling them to participate in abiotic reduction of inorganic arsenate to arsenite.[8] In addition, the redox-active mineral mackinawite (FeS) was shown to simultaneously reduce As(V) and U(VI) in U-/As-coexisting aqueous systems.[9] However, most of the reported investigations for arsenate reduction were carried out in the aqueous phase, whereas surface reactions in nonsaturated aqueous systems remain largely unexplored. For instance, paddy soil during the drying period and soil around industrial sites are two typical examples of nonsaturated aqueous systems, where microbial activity is typically suppressed due to low moisture levels. Previous studies suggest that the surface reactions of pollutants in nonsaturated aqueous states differ from those in the aqueous phase. Jin et al. found that chloramphenicol, a typical antibiotic commonly found in environment, could be degraded through abiotic hydrolysis on phyllosilicate and iron(III) (oxyhydr)oxide mineral surfaces in the nonaqueous phase while showing no degradation in the aqueous phase.[10,11] Xu et al. confirmed that the decomposition rate of polydimethylsiloxanes on clay mineral surfaces in a drought environment was faster than that under aqueous conditions.[12] These results indicate that the abiotic pathway under drought conditions is a long-overlooked but very important process influencing the migration and transformation of pollutants.

Fe(III) (oxyhydr)oxide minerals are common and significant components of soil due to their high reactivities and large abundance in the earth's crust, playing a crucial role in controlling the mobility and toxicity of As in contaminated soils.[13] Although the reduction of As(V) to As(III) on As-bearing iron minerals in aqueous systems has been extensively investigated, the possibility of As(V) reduction on dry iron minerals under drought conditions remains poorly understood. In this study, ferrihydrite, a typical Fe(III) oxyhydroxide commonly found in soils, was employed to examine the reduction of As(V) to As(III) for understanding its natural transformation in a drought environment. The objectives of this study were (1) to evaluate the As(V) reduction on iron minerals under drought conditions; (2) to investigate the factors that may affect As(V) reduction; and (3) to elucidate the underlying mechanism of As(V) reduction to As(III) on iron mineral surfaces in a drought environment.

2. EXPERIMENTAL SECTION

2.1. Iron Minerals and Chemicals. Ferrihydrite (denoted as Fh) was synthesized using a coprecipitation approach as reported by Schwertmann and Cornell.[14] First, a 1 M NaOH solution was used to adjust the pH of a $Fe(NO_3)_3$ solution (0.1 M, 500 mL) to 7−8. After 2 h, the obtained precipitate was washed several times, freeze-dried, and stored at 4 °C. For comparison, two other iron minerals, hematite and magnetite, were also used in this study. Analytical grade magnetite (denoted as Mag) was procured from Sigma Biochemical Technology Co., Ltd., China, and used without further treatment. Hematite (denoted as Hem) was prepared according to a method described previously.[15] XRD patterns and SEM images of the three iron minerals are presented in Figure S1. A detailed preparation procedure for hematite is shown in Text S1.

2.2. As(V) Reduction under Drought Conditions. The experiments of As(V) reduction by iron minerals under drought conditions were carried out in the dark. First, As(V) stock solutions (5 mL, 13.3 mM) were added to 1.0 g L^{-1} mineral suspensions (200 mL) to guarantee saturated adsorption of As(V) on the surface of the minerals. The pH of the suspensions was adjusted to 6.0 by using 0.1 M HCl and 0.1 M NaOH. After 24 h, the As(V)-adsorbed iron minerals were separated from the suspensions by using a 0.22 μm membrane filter. Subsequently, the wet mineral solids were rapidly transferred to an anoxic glovebox and an air-exposed glass desiccator, respectively. At specified time intervals from 0 to 60 days, the minerals were collected, packed into valve bags to remove air, and stored in a −20 °C freezer for further analysis. High-resolution X-ray photoelectron spectroscopy (XPS) analysis was utilized, as it is a nondestructive method suitable for determining the oxidation state of surface elements. In addition, the content of structural Fe(II), As(III), and total As in solids was analyzed during the experiments. The suspensions were collected to detect the arsenic concentrations for calculating the amount of As sorbed on the iron minerals. To reveal the effect of initial solution pH on the reduction of As(V), the solution pH of suspensions was adjusted to the target values of 5.0 ± 0.1, 7.0 ± 0.1, and 9.0 ± 0.1 using HCl and NaOH, which represented acidic, neutral, and basic conditions, respectively. To illustrate the effect of the atmosphere on the As(V) reduction by iron minerals, the As(V)-adsorbed iron mineral solids were placed in a quartz tube to inject nitrogen, air, or oxygen, respectively. Since wet minerals required more than 3 days to dry at room temperature, we used elevated temperatures to speed up the drying process and better investigate the atmospheric effects on the reduction of As(V) by iron minerals. To achieve this, the quartz tube was heated to 60 °C for 12 h. Unless otherwise specified, all experiments were conducted at room temperature.

2.3. Sample Characterization. The phase structure of iron minerals was analyzed by X-ray diffraction (XRD) on a Bruker D8 ADVANCE X-ray diffractometer using Ni-filtered Cu Kα radiation. The high-resolution As 3d and Fe 2p XPS spectra of minerals were collected using a Sigma Probe system (Thermo) with an Al Kα X-ray source (1486.7 eV) having 75 W source power. Shirley baseline and a Gaussian−Lorentzian peak shape were used for fitting the As 3d and Fe 2p XPS data. High-resolution As 3d spectra obtained in the range of 42−48 eV were used to identify the redox states of As. We also performed an angle-resolved XPS (ARXPS) test for collecting Fe 2p regions in the range of 700−740 eV with electron emission angles of 30° and 60°, respectively. The C 1s peak at 284.8 eV was used as a reference to correct the surface charging effects. The charge resistivity of mineral powders was measured using the four-point probe method. Mössbauer spectroscopy measurements were performed at different temperatures using a Mössbauer spectrometer (Germany, Wissel MS-500) in transmission geometry with constant acceleration mode. Positron annihilation lifetime (PAL) spectroscopy data of iron minerals were collected on an EG&G ORTEC fast−fast coincidence system with a resolution of 210 ps. Detailed characterizations are presented in Text S2.

2.4. X-ray Absorption Spectra (XAS) Measurement. The Fe L-edge XAS spectra of samples were collected at the BL12B beamline in the Hefei Synchrotron Radiation Light Source (HLS, China). The As (11 867 eV) K-edge XAS spectra of samples were measured at the 1W1B beamline in the Beijing Synchrotron Radiation Facility (BSRF, China).

https://doi.org/10.1021/acs.est.4c10674
Environ. Sci. Technol. 2025, 59, 5191−5201

Fluorescence mode was employed to acquire As K-edge XAS spectra at room temperature. Energy calibrations of As were conducted to overcome the energy shift problem by the first inflection points of Au metal foil absorption edges, which were determined by their first derivatives (As = 11 867 eV).[16] Background, energy corrections, and normalization of raw As K-edge XANES data were performed by using Athena software programs. To analyze the As oxidation state of As-adsorbed iron minerals, the normalized As K-edge XANES spectra were fitted using linear combination fitting (LCF). The spectra of sodium arsenate (NaH_2AsO_4, As(V)) and sodium arsenite ($NaAsO_2$, As(III)) were measured as standards for LCF analysis.

2.5. Analysis of As Species and Structural Fe(II) in Minerals. The solid particles were dispersed in a 10 mL centrifuge tube using an ultrasonic bath for 10 min. Subsequently, 2 mL of the suspension was taken for As and Fe species analysis. The method for extracting As species referred to in this study follows the procedure outlined in previous work.[17] Briefly, a 2 mL suspension sample was added to a solution containing H_3PO_3, $NH_2OH{\cdot}HCl$, and H_2O and allowed to react for 10 min. The mixture was then centrifuged at 11 000 rpm for 10 min. The resulting supernatant was filtered through a sterile 0.22 μm filter. The concentration of As(III) was quantified using high performance liquid chromatography coupled to atomic fluorescence spectroscopy (SA-20, Jitian, Beijing, China). The total As concentration was quantified by an inductively coupled plasma optical emission spectrometer (ICP-OES). The detailed analysis of As is shown in Text S3. The concentration of structural Fe(II) in iron minerals ($Fe(II)_{stru}$) was indirectly obtained through analyzing their concentrations of total Fe (Fe_T), aqueous Fe(II) ($Fe(II)_{aq}$), and Fe(II) adsorbed on minerals ($Fe(II)_{sorb}$). Structural Fe(II) was calculated as follows: $[Fe(II)_{stru}] = [Fe(II)_{total}] - ([Fe(II)_{aq}] + [Fe(II)_{sorb}])$. The extraction approaches for $Fe(II)_{tot}$, $Fe(II)_{aq}$, and $Fe(II)_{ads}$ used in this study were based on previous work.[18] The detailed analysis of Fe species is explained in Text S4.

2.6. DFT Calculations. DFT calculations were performed using the Vienna Ab initio Simulation Package (VASP) with the Perdew–Burke–Ernzerhof (PBE) exchange-correlation functional and a plane-wave cutoff energy of 500 eV. The projector augmented wave (PAW) pseudopotentials were used for DFT calculations. The valence electrons for Fe, O, As, and H atoms were set as 8, 6, 5, and 1, respectively.[19] DFT-D_3 correction with the Grimme scheme was used to account for the dispersion interaction. The on-site Coulomb repulsion of Fe 3d electrons was treated by the DFT + U approach, where U_{eff} is equal to 4.0 eV,[20] and the structural convergence is set to a force tolerance of 0.01 eV/Å and an energy tolerance of 1.0×10^{-5} eV. The bulk unit cell of ferrihydrite was $a = c =$ 11.856 Å, $b = 25$ Å and $\alpha = \gamma = 90°$, $\beta = 120°$. A (001) facet with four atomic layers of Fe and more than 15 Å of vacuum region along the b-direction was constructed. The (001) surface was cleaved from the optimized bulk structure of a $2 \times 2 \times 1$ supercell. The $H_2AsO_4^-$ ions were employed as As(V) species for DFT calculations. Adsorption energy (E_{ads}) was calculated as follows:[15,16]

$$E_{ads} = E_{Fh+As(V)} - E_{Fh} - E_{As(V)}$$

where E_{Fh} and $E_{As(V)}$ represent the energies of the ferrihydrite slab and the As(V) ion, respectively, and $E_{Fh+As(V)}$ is the total energy of the slab with adsorbed As(V). The charge transfer between Fe and As atoms was investigated based on Bader's charge analysis program.[19,21]

3. RESULTS AND DISCUSSION

3.1. As(V) Reduction on the Surface of Ferrihydrite under Drought Conditions. Figure 1a and Table S1 illustrate the evolution of the oxidation state of arsenic adsorbed on ferrihydrite, as determined by high-resolution As 3d XPS, under drought conditions. As_2O_3 and $Na_3AsO_4{\cdot}7H_2O$ powders were used as standards for As(III) and As(V), respectively (Figure S2). The calculated amount of As(V) adsorbed on ferrihydrite was 487.0 μmol g^{-1} (Figure S3). At day 0, the As 3d XPS spectrum of As(V) adsorbed on ferrihydrite was very similar to that of the $Na_3AsO_4{\cdot}7H_2O$ powder (Figure 1a), and no new peak attributed to As(III) species appeared. Additionally, we examined the change in As oxidation state after As(V) reacted with ferrihydrite under air-exposed aqueous conditions for 60 days (Figure S4). We did not observe As(III) species in the As 3d XPS spectrum of As(V) adsorbed on ferrihydrite under aqueous conditions, indicating that As(V) reduction by ferrihydrite did not occur in an aqueous environment, consistent with previous findings.[22] Interestingly, as the As(V)-adsorbed ferrihydrite solids became dry, a new peak at ~44.5 eV, which can be assigned to As(III), occurred in the As 3d XPS spectrum. After 7 days, 40.8% of As(V) sorbed on ferrihydrite was reduced to As(III) under anoxic conditions. Furthermore, we also observed the As(III) species in the As 3d XPS spectrum of As(V)-adsorbed ferrihydrite solids after 30 and 60 days (Figure 1a and Figure S5), with the reduction percentage of adsorbed As(V) remaining at 35.9% and 39.4%, respectively. This result

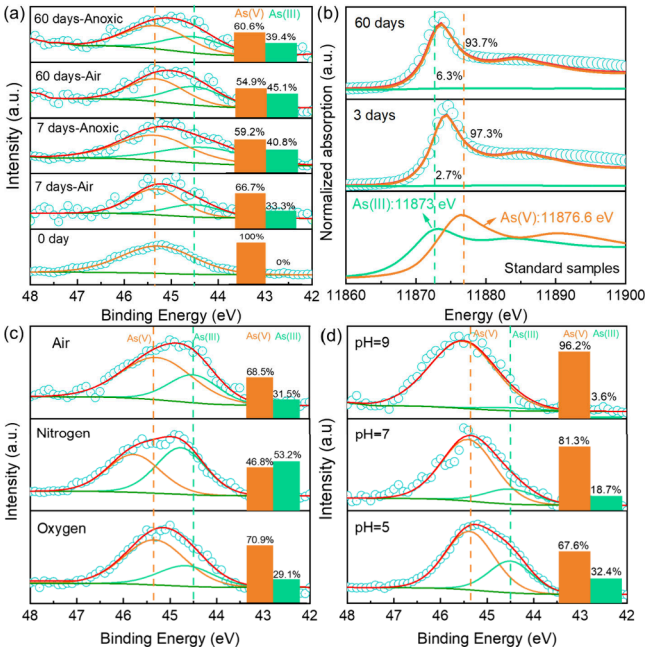

Figure 1. Evolution of the oxidation state of As species adsorbed on ferrihydrite measured by high-resolution As 3d XPS (a) and As K-edge XANES (b). The effect of atmosphere (c) and initial pH (d) on the As(V) reduction on dried ferrihydrite powders after 30 days. All experiments were carried out under drought conditions. Green open circles and red solid lines represent the experimental and fitting data, respectively.

https://doi.org/10.1021/acs.est.4c10674
Environ. Sci. Technol. 2025, 59, 5191−5201

indicates that the formed As(III) could exist stably on the ferrihydrite surface. As K-edge XANES spectra of the dried As(V)-adsorbed ferrihydrite were collected (Figure 1b), as the XANES technique allows one to determine the oxidation state of sorbed arsenic. Linear combination fitting (LCF) results revealed that 2.7% of As(V) was reduced to As(III) after 3 days, while 6.3% of As(III) was detected after 60 days. In general, XANES analysis captures signals from arsenic adsorbed on both the external surfaces and interior of minerals, while XPS analysis is surface-specific, probing depths of less than 10 nm. As a consequence, the surface-sensitive XPS analysis detects a strong As(III) signal, while the bulk As(III) analysis by XANES is diluted. This phenomenon has been also reported in previous studies, where it was observed that the As redox signature detected by XANES analysis was lower than that detected by XPS analysis.[23,24] Although the amount of As(III) detected by XANES analysis was less than that detected by high-resolution XPS analysis, it also clearly demonstrated that the reduction of As(V) to As(III) occurred under anoxic conditions in a drought environment. Surprisingly, the reduction of As(V) to As(III) on the ferrihydrite surface was also observed in an air-exposed atmosphere (Figure 1a and Figure S5). After 7 and 60 days, the proportion of As(III) on ferrihydrite reached 33.3% and 45.1% of the total sorbed As, respectively (Figure 1a).

To further illustrate the effect of atmospheric composition on As(V) reduction, the evolution of the As oxidation state was followed in nitrogen, air, and oxygen atmospheres (Figure 1c), respectively. We observed As(V) reduction in an 100% oxygen atmosphere (29.9% As(III)), although it was not as pronounced as that in air (32.0% As(III)) and nitrogen (53.0% As(III)). Additionally, As(V) reduction occurred under acidic (pH 5), neutral (pH 7), and alkaline (pH 9) conditions in an anoxic glovebox within 30 days, showing As(V) reduction percentages of 32.4%, 18.7%, and 3.6%, respectively (Figure 1d). The extent of reduction under acidic and neutral conditions was significantly higher than that under alkaline conditions, suggesting that pH was a key factor influencing As(V) reduction. To sum up, high-resolution XPS and XANES analyses clearly demonstrated the abiotic reduction of As(V) by ferrihydrite under both anoxic and oxic conditions across a wide pH range in a drought system.

3.2. As(V) Reduction by Hematite and Magnetite. The question resulting from these initial observations is, why does the reduction of As(V) to As(III) spontaneously occur on the surface of poorly crystalline ferrihydrite during the drying process? Previous reports have confirmed that dissolved and/or sorbed Fe(II) species could act as reducing agents, facilitating the transformation of ferrihydrite-bound As(V) to As(III) in aqueous systems under anoxic conditions.[7] However, we did not add exogenous Fe(II) or any reducing chemicals (e.g., reducing natural organic matter or sulfide) to our experiments. Therefore, we could exclude the possible contribution of adsorbed Fe(II) species to the observed As(V) reduction. To investigate whether structural Fe(II) acts as an electron donor in As(V) reduction, we conducted comparative experiments using two additional iron minerals, hematite and magnetite, under drought conditions at pH 6.0 in an anoxic glovebox. Hematite is a well-crystallized iron(III) oxide (Fe_2O_3) containing primarily Fe(III), whereas magnetite (Fe_3O_4) is a mixed-valent mineral containing Fe(II) and Fe(III). The amounts of As(V) adsorbed on hematite and magnetite were 7.3 and 15.6 μmol g^{-1}, respectively (Figure S3). As shown in Figure 2a, the As 3d spectra of As(V) adsorbed on hematite and magnetite samples at day 0 could

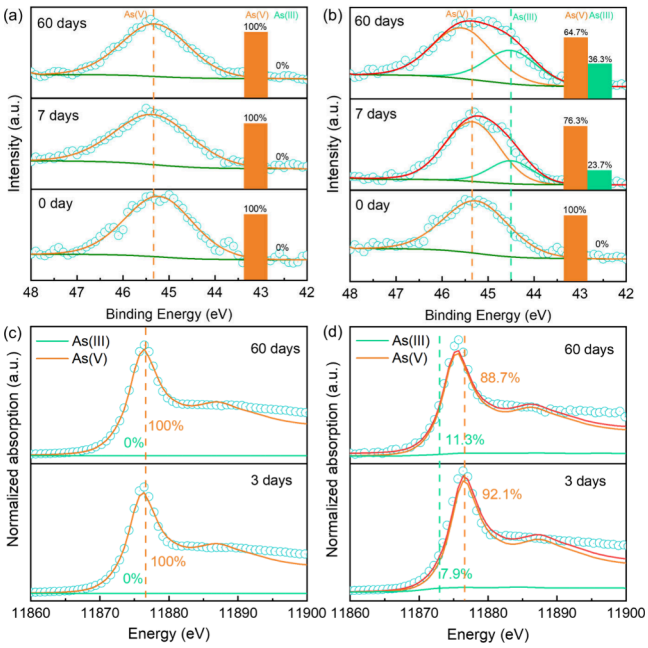

Figure 2. Evolution of redox state of As(V) adsorbed on hematite (a, c) and magnetite (b, d) determined by high-resolution As 3d XPS and As K-edge XANES. All experiments were carried out under drought conditions. Green open circles and red solid lines represent the experimental and fitted data, respectively.

only be fitted with a peak at ~45.4 eV, which was attributed to As(V). After 7 days, we observed both As(III) and As(V) species on the magnetite surface (Figure 2b and Table S2). After 30 and 60 days, the fraction of As(III) increased from 23.7% (day 7) to 28.1% and 36.3%, respectively (Figure 2b and Figure S6). In contrast, the As 3d spectra of hematite with adsorbed As(V) showed no obvious changes after 7 days compared to day 0. Even after 60 and 100 days, only As(V) species were observed on the hematite surface (Figure 2a and Figure S6). These results were further confirmed by As K-edge XANES analysis. The LCF results showed that no As(III) species were detected after 3 and 60 days for hematite (Figure 2c), whereas 7.9% and 11.3% As(III) were observed after 3 and 60 days for magnetite, respectively (Figure 2d). As As(V) reduction did not occur in experiments with hematite but did occur with magnetite, structural Fe(II) in iron minerals most likely played a vital role in As(V) reduction.

3.3. Evolution of Fe Oxidation State versus As(V) Reduction. ARXPS is a sensitive tool to detect the oxidation state of elements in mineral samples at varying depths relative to the mineral surface. To confirm whether structural Fe(II) mediates the observed As(V) reduction, we analyzed the evolution of the Fe oxidation state in different As(V)-adsorbed iron minerals within the surface depths of ~3.5 and ~10 nm, respectively (Table S3). As shown in Figure 3a, the Fe 2p XPS spectra of As(V)-adsorbed ferrihydrite after 30 days could be divided into eight peaks. The binding peaks at ~710.15 and ~723.35 eV with two satellite peaks at ~713.90 and ~727.12 eV were attributed to Fe(II) species, while the binding peaks at ~711.46 and ~724.80 eV with two satellite peaks at ~717.53 and 719.80 eV corresponded to Fe(III) species.[25−27] Remarkably, the calculated Fe(II)/Fe(III) molar ratios in

https://doi.org/10.1021/acs.est.4c10674
Environ. Sci. Technol. 2025, 59, 5191−5201

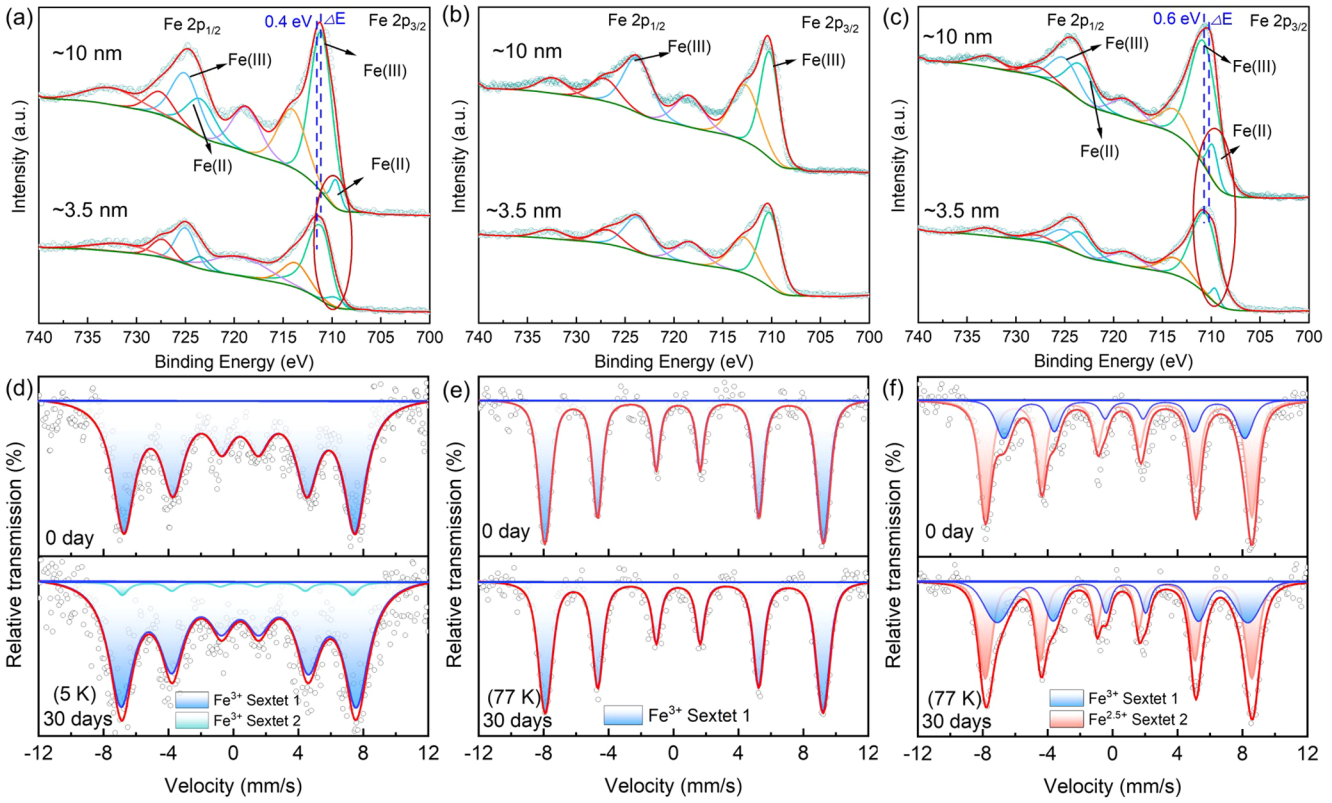

Figure 3. Evolution of Fe oxidation state of As(V)-adsorbed ferrihydrite (a), hematite (b), and magnetite (c) powders within depths of ∼3.5 and ∼10 nm, respectively. Mössbauer spectra of As(V)-adsorbed ferrihydrite (d), hematite (e), and magnetite (f) powders at initial day 0 and after 30 days. The experimental data points are represented by empty circles (a−c) and black points (d−f). White open circles and red solid lines represent the experimental and fitted data, respectively.

Table 1. Fitting Parameters of Mössbauer Spectra for Different As(V)-Adsorbed Iron Minerals before and after 30 Days

samples	reaction time (days)	components	relative area (%)	CS[a] (mm s^{-1})	QS or ε[b] (mm s^{-1})	H[c] (T)	σ[d] (mm s^{-1})	red-χ^2[e]
Fh	0	Fe^{3+} sextet 1	100	0.40	−0.04	44.28	1.67	1.26
	30	Fe^{3+} sextet 1	95.2	0.39	−0.09	45.11	1.88	1.02
		Fe^{3+} sextet 2	4.8	0.31	−0.06	44.18	0.88	
Hem	0	Fe^{3+} sextet 1	100	0.48	0.18	53.25	1.61	0.76
	30	Fe^{3+} sextet 1	100	0.48	0.18	53.09	1.67	0.70
Mag	0	Fe^{3+} sextet 1	57.7	0.37	0.02	50.97	1.65	0.62
		$Fe^{2.5+}$ sextet 2	42.3	0.74	−0.10	47.95	4.10	
	30	Fe^{3+} sextet 1	70.9	0.40	0.00	51.00	1.06	1.07
		$Fe^{2.5+}$ sextet 2	29.1	0.75	0.01	46.09	2.00	

[a]Center shift. [b]Quadrupole shift (for sextets). [c]Hyperfine field. [d]σ, standard deviation of sextet. [e]Red-χ^2, goodness of fit.

ferrihydrite within a depth of ∼3.5 nm (0.07) was considerably lower than that within a depth of ∼10 nm (0.14). The relatively low Fe(II)/Fe(III) molar ratios within a depth of ∼3.5 nm compared to those within ∼10 nm suggest that surface structural Fe(II) in ferrihydrite was involved in As(V) reduction, leading to the consumption of surface Fe(II). The Fe 2p XPS spectra of As(V)-adsorbed hematite and magnetite samples showed similar profiles as the spectra collected for ferrihydrite (Figure 3b,c). However, the evolution of the Fe(II)/Fe(III) molar ratios varied within different depths for the three minerals after reacting with As(V) for 30 days. For hematite, we did not detect any Fe(II) species within depths of ∼3.5 and ∼10 nm, suggesting that no redox reaction occurred on the hematite surface. In contrast, magnetite, which contains both Fe(II) and Fe(III), showed trends similar to those of ferrihydrite, i.e., the Fe(II)/Fe(III) molar ratio within the depth of ∼3.5 nm decreased to 17.1% compared to that within the depth of ∼10 nm (21.5%).

The evolution of the Fe oxidation state in the three investigated iron minerals before and after the reaction with As(V) was also recorded by Mössbauer spectroscopy (Table 1). As shown in Figure 3f, the Mössbauer spectra of magnetite before and after reaction with As(V) for 30 days could be well resolved using two sextets, i.e., one primary sextet (blue line) and one small sextet (pink line), appearing as a shoulder on the primary sextet. The primary sextet had a center shift (CS) of 0.37−0.40 mm s^{-1} and quadrupole splitting (QS) of 0.00−0.02 mm s^{-1}, which was attributed to the tetrahedral Fe^{3+} ($^{Tet}Fe^{3+}$) sites in magnetite.[28] The small sextet was assigned to the octahedral Fe^{2+} and Fe^{3+} sites with an average valence state of 2.5 ($^{Oct}Fe^{2.5+}$), as evidenced by its CS of 0.75−0.74 mm s^{-1} and QS of −0.01 to −0.10 mm s^{-1}.[28,29] The relative peak area

https://doi.org/10.1021/acs.est.4c10674
Environ. Sci. Technol. 2025, 59, 5191−5201

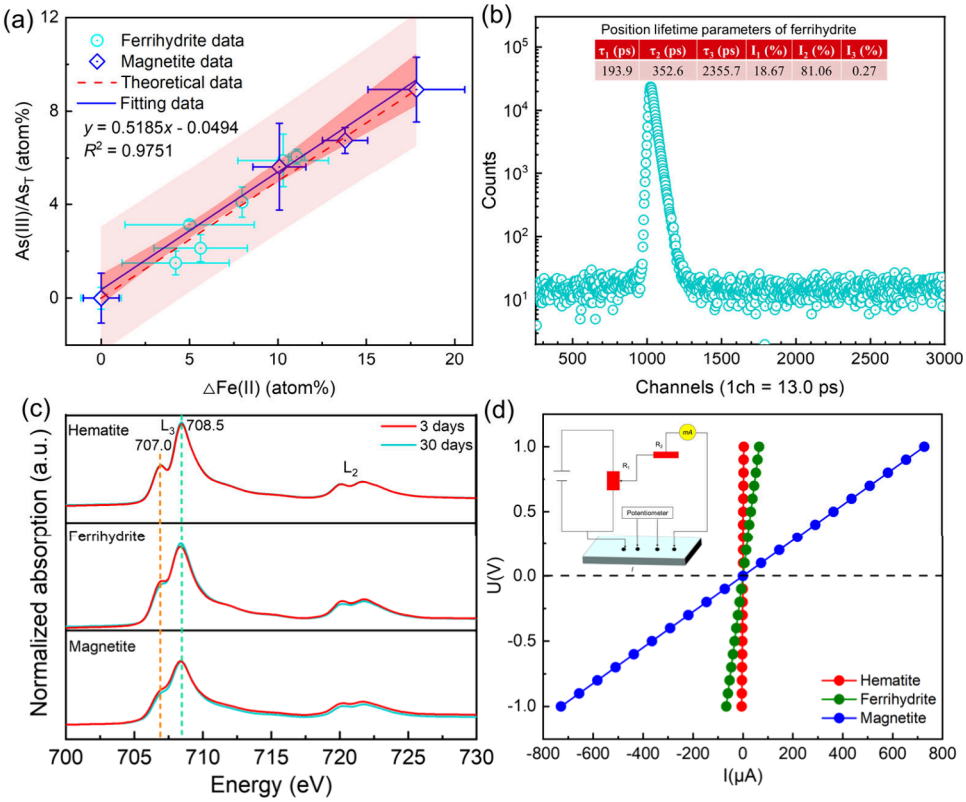

Figure 4. Evolution of the amount of As(III) species (atom%) as a function of Fe(II) content (atom%) in As(V)-adsorbed ferrihydrite and magnetite systems under drought conditions (a). Peak-normalized positron annihilation lifetime spectrum of ferrihydrite (inset is the fitting parameters) (b). Fe L-edge XANES spectra (c) and charge resistivity (d) of iron (oxyhydr)oxides powders. A schematic diagram of the four-point probe method for measuring the charge resistivity of iron minerals is included in (d).

of $^{Oct}Fe^{2.5+}$ in magnetite after reacting with As(V) for 30 days was 29.1%, which was obviously lower than that at the initial day 0 (42.3%), suggesting that structural Fe(II) in magnetite was oxidized to Fe(III) after reaction with As(V), which was in agreement with the result of ARXPS analysis. In addition, the Mössbauer spectra of hematite before and after reaction with As(V) could be well fitted with a single sextet (Figure 3e), corresponding to high-spin octahedral Fe^{3+} ($^{Oct}Fe^{3+}$) sites.[30−32] This result combined with the ARXPS analysis revealed that hematite was very stable during the entire reaction and consisted only of Fe(III). Remarkably, Fe(II) species were not found in the Mössbauer spectrum of ferrihydrite at day 0 (Figure 3d). This may be due to the relatively low sensitivity of Mössbauer spectroscopy (5−10% for certain Fe species) compared to ARXPS, which is more surface-sensitive. Nonetheless, we observed phase transformations in ferrihydrite to other iron minerals (e.g., lepidocrocite) after 30 days (Figure 3d, Figure S7, and Table S4), although the transformation was not easily detected by XRD due to the low content (<5%) of these phases (Figure S8). Theoretically, ferrihydrite is relatively stable in anoxic environments.[33] Moreover, the presence of adsorbed As(V) was shown to further retard the transformation of ferrihydrite.[34,35] However, the phase transformation of ferrihydrite after 30 days, observed in an anoxic glovebox, suggested a redox reaction between As(V) and ferrihydrite, as supported by the corresponding ARXPS data. This result reveals that the transformation of As(V) to As(III) was coupled to the oxidation of structural Fe(II) to Fe(III).

To further reveal the possible relationship between the oxidation of structural Fe(II) and the reduction of As(V), we quantified the changes in structural Fe(II) and the formation of As(III) species in ferrihydrite and magnetite systems over a reaction period of 0 to 60 days using wet chemical analysis (Table S5). The correlation between the increasing amount of As(III) and the decreasing Fe(II) content is illustrated in Figure 4a, where y represents the increase in As(III) species (As(III)/As(T), atom%) and x denotes the decrease in structural Fe(II) (atom%) in As(V)-adsorbed iron minerals. Theoretically, the production of 1 mol of As(III) requires the consumption of 2 mol of Fe(II). Interestingly, the fitted slope (0.519) of the increased amount of As(III) species as a function of the decreased Fe(II) species was very close to the theoretical value of 0.5 (Figure 4a). This strong correlation indicates that structural Fe(II) species on the surface of ferrihydrite drove the reduction of As(V) in a drought system.

3.4. Origin of Structural Fe(II) in Ferrihydrite. The ferrihydrite used in this study was synthesized from a Fe(III) salt and consequently is expected to contain only Fe(III). The reason ferrihydrite nevertheless possesses Fe(II) in its structure can be explained as follows. Some researchers have reported that ferrihydrite exhibits weak ferrimagnetism at room temperature,[36,37] indicating that the net magnetic moment within the ferrihydrite structure is not entirely canceled out. Due to the extremely small crystallite size of approximately 2−6 nm,[38−40] the weak ferrimagnetism of ferrihydrite was often attributed to uncompensated surface spins resulting from nanoparticle interactions.[37,41] However, the mechanism of nanoparticle interactions did not fully explain the evolution of magnetism in ferrihydrite observed in previous studies. For instance, Wang et al. observed size-dependent magnetic

https://doi.org/10.1021/acs.est.4c10674
Environ. Sci. Technol. 2025, 59, 5191−5201

properties in ferrihydrite, noting that both the magnetization and the coercivity of two-line ferrihydrite decreased as the crystallite size increased.[42] In contrast, Michel and co-authors found that ordered ferrihydrite (with relatively large crystallite particles) was more prone to exhibit weak ferrimagnetism compared to disordered ferrihydrite (with smaller crystallite particles).[43] In addition to the small particle size, a disordered arrangement of surface atoms is another typical characteristic of poorly crystalline ferrihydrite, which has been widely reported in previous work.[38,42] In this case, vacancy defects, such as cationic Fe vacancies and oxygen vacancies, are most likely to form on the disordered surface of ferrihydrite, potentially contributing to its weak ferrimagnetism at room temperature. For instance, the presence of cation Fe vacancies could disrupt the antiferromagnetic symmetry of iron minerals (e.g., goethite),[44] thereby showing weak magnetic moments. However, ordered ferrihydrite exhibited fewer cation Fe vacancies in its structure compared to disordered ferrihydrite, yet it displayed a relatively stronger ferrimagnetism than the latter. These results indicate that cation Fe vacancies and particle size may not be the primary contributors to the weak ferrimagnetism of poorly crystalline ferrihydrite.

Notably, oxygen vacancy defects in ferrihydrite are more likely to form compared to Fe vacancies. This is because oxygen atoms are located on the outer spheres of the Fe−O tetrahedral and octahedral units in ferrihydrite, with each Fe atom surrounded by five and six oxygen atoms in the tetrahedral and octahedral units, respectively. Consequently, the formation of a single Fe vacancy could lead to the generation of two or more oxygen vacancies on the ferrihydrite surface. Previous studies had reported that the presence of oxygen vacancies influenced the Fe oxidation state of iron minerals, resulting in its shift to a lower value for maintaining electrostatic balance:[15]

$$-Fe^{3+}-O^{2-}-Fe^{3+}-O^{2-}-Fe^{3+}- \rightarrow -Fe^{3+}-O^{2-}-Fe^{3+}-\square-Fe^{3+} + \frac{1}{2}O_2 \quad (1)$$

where the hollow block □ represents the oxygen vacancy defects in the structure of iron(III) minerals. The reaction described above can be written as follows:

$$FeOOH \rightarrow Fe_y^{3+}Fe_{1-y}^{2+}O_{2-x}^{2-}H + \frac{x}{2}O_2 \quad (2)$$

where y and $1 - y$ are the fraction of Fe^{3+} and Fe^{2+} species in iron oxyhydroxides, respectively, and x is the concentration of oxygen vacancy defects. From eq 2, it can be seen that oxygen vacancy defects are closely linked to the Fe oxidation state in ferrihydrite, i.e., the greater the number of oxygen vacancy defects, the more Fe(II) is present in the structure of ferrihydrite. Interestingly, ferrihydrite treated with Fe(III)-reducing bacteria has been found to produce more structural Fe(II) species within the mineral solid. These Fe(II) species significantly impact magnetic susceptibility, which increases as the solid Fe(II)/Fe(III) ratio rises.[45] Therefore, the weak ferrimagnetism observed in ferrihydrite may be attributed to the formation of structural Fe(II), which is facilitated by the presence of oxygen vacancy defects.

To further reveal whether oxygen vacancy defects occur in the structure of poorly crystalline ferrihydrite, we applied positron annihilation lifetime (PAL) spectroscopy, a unique and sensitive probe for identifying defects in minerals. The PAL spectrum of ferrihydrite could be decomposed into three distinct lifetime components: τ_1, τ_2, and τ_3 (Figure 4b). The τ_1 component (193.9 ps) corresponded to the free annihilation of positrons in the defect-free bulk regions and/or smaller vacancies in disordered minerals.[46−48] The τ_2 component (352.6 ps) was attributed to the positrons captured by large size defects (e.g., oxygen vacancy clusters) in the minerals.[47] The τ_3 component, with a lifetime of 2335.7 ps, was associated with the annihilation of *ortho*-positronium inside the large voids of minerals.[47,49] According to the analysis described above, τ_2 components could be used as evidence of oxygen vacancy defects in ferrihydrite. As shown in Figure 4b, the intensity of the τ_2 component (I_2) was the largest (81.1%), followed by the intensity of the τ_1 (I_1, 18.7%) and τ_2 (I_3, 0.2%) components, indicating the presence of abundant oxygen vacancy defect clusters in the structure of ferrihydrite. This clearly demonstrated that oxygen vacancy defects in ferrihydrite with relatively low crystallinity played a crucial role in forming structural Fe(II) to maintain electrostatic balance, which also explained why we observed Fe(II) species in ferrihydrite using high-resolution XPS and chemical chromogenic analysis (Figure S9). Moreover, Michel et al. proposed a new chemical composition of $Fe_{8.2}O_{8.5}(OH)_{7.4} + 3H_2O$ for ferrihydrite,[43] which emphasized the nonstoichiometric iron and oxygen contents in the structure of poorly crystalline ferrihydrite, revealing the coexistence of oxygen vacancies and Fe vacancies. Based on the new chemical composition, the calculated Fe oxidation state (2.97) in ferrihydrite was slightly lower than the theoretical Fe oxidation state of +3, suggesting the presence of low-valence Fe species (e.g., Fe(II)) within the ferrihydrite structure. This observation aligned with and supported our findings.

3.5. Electron Transfer between As(V) and Iron (Oxyhydr)oxides under Drought Conditions. We observed the reduction of As(V) to As(III) by ferrihydrite under drought conditions. However, the underlying electron transfer mechanism between ferrihydrite and As(V) remains unclear. Fe L-edge XANES spectroscopy, which probes the excitation of 2p electrons into unoccupied 3d states, provides a resolution that is 3−5 times higher than that of Fe K-edge XANES.[50−52] Therefore, Fe L-edge XANES can provide more detailed information about the electronic changes associated with valence orbitals during the chemical reaction between iron minerals and As(V). As shown in Figure 4c, two distinct peaks of high energy at ∼708.5 eV and relatively low energy at ∼707.0 eV were observed in the Fe L_3-edge XANES spectra of ferrihydrite with adsorbed As(V), which correspond to the transition from Fe $2p_{3/2}$ to the Fe 3d unoccupied state.[50] The intensity ratio of the high-energy peak (∼708.5 eV) to the low-energy peak (∼707.0 eV) for ferrihydrite after reacting with As(V) was 1.53 at day 3 but increased to 1.66 after 30 days (Table S6). This result indicates that the low-energy unoccupied Fe 3d state, corresponding to Fe^{2+} ($3d^6$) species, gradually became less after reacting with As(V) (e.g., 30 days), leading to an increase of structural Fe(III) species in the ferrihydrite. For comparison, we also collected Fe L-edge XANES spectra of hematite and magnetite (Figure 4c). The spectral profiles of these minerals were similar to that of ferrihydrite, but the evolution of high-energy to low-energy peak intensity ratios differed. For hematite, the intensity ratio of high-energy to low-energy peaks after reacting with As(V) for 30 days (1.72) was very close to that at initial day 3 (1.73), indicating that the local electron structure of Fe atoms in hematite did not change. Remarkably, the intensity ratio of

https://doi.org/10.1021/acs.est.4c10674
Environ. Sci. Technol. 2025, 59, 5191−5201

high-energy to low-energy peaks for magnetite shifted from 1.53 to 1.67 after 30 days, suggesting an increase in the structural Fe(III) species after reaction with As(V). The decrease of the low-energy unoccupied Fe 3d state in ferrihydrite and magnetite indicates that electron transfer from Fe to As atoms occurred during the interactions between As(V) and Fe minerals under drought conditions.

We measured the charge resistivity of iron mineral powders using the four-point probe technique to assess the interfacial electron transfer kinetics in a drought environment (Figure 4d). Hematite showed an extremely large charge resistivity of 6734.1 Ω·m, indicating that charge transfer in Fe(III) mineral was very difficult. This was the reason why we did not observe As(V) reduction by hematite under drought conditions. Compared to hematite, magnetite, containing both Fe(II) and Fe(III), showed low charge resistance, i.e., 44.3 Ω·m. The relatively low charge resistance in magnetite was beneficial to the charge transfer between the mineral and As(V), thereby promoting As(V) reduction. Although the charge resistance of ferrihydrite (485.1 Ω·m) was higher than that of magnetite, it remained lower than that of hematite. This result revealed that the presence of structural Fe(II) lowered the charge resistance, enabling electron transfer between ferrihydrite and adsorbed As(V).

To further reveal the occurrence of electron transfer between ferrihydrite and As(V) under drought conditions, we employed DFT calculation to investigate the evolution of the valence electron of As and Fe atoms in the ferrihydrite-As(V) system using Bader charge analysis (Table S7). Solvation parameters were excluded from all DFT calculations. In general, ferrihydrite contains two types of Fe sites (Figure 5a). The first is a saturated-coordinated Fe site, where six oxygen atoms are bound to form a Fe−O octahedron (green atom, labeled as Fe_{Oh}). The second is an undercoordinated Fe site, where four oxygen atoms are bound to form a Fe−O tetrahedron (blue atom, labeled as Fe_{Th}). According to previous reports, tetrahedral and octahedral Mn sites in hausmannite are associated with Mn(II) and Mn(III), respectively.[19] Although the structures of hausmannite and ferrihydrite differ, they share some similar characteristics. For example, they are composed of MeO_4 tetrahedra and MeO_6 octahedra units. In this study, Fe_{Oh} and Fe_{Th} therefore represent structural Fe(III) and Fe(II) sites in ferrihydrite, respectively (Figure 5a). The $H_2AsO_4^-$ ion was used as the As(V) chemical model because it is the predominant species in the typical pH range of 4 to 7. Figure 5b,c illustrates the schematic model of As(V) species absorbed on the surface Fe_{Oh} and Fe_{Th} sites of ferrihydrite. The calculated adsorption energies (E_{ads}) of $H_2AsO_4^-$ on the Fe_{Th} and Fe_{Oh} sites were −1.11 and −1.50 eV, respectively, indicating that As(V) species had a strong affinity to the ferrihydrite surface. In addition, the local electron density of the As−O−Fe complex on the Fe_{Oh} site of ferrihydrite was obviously different from that on the Fe_{Th} site after As(V) adsorption. The electron cloud significantly concentrated around the As atom in the As−Fe_{Th} complex, whereas this phenomenon was not observed in the As−Fe_{Oh} complex (Figure 5b,c). The charge accumulation observed in the As atom adsorbed on the Fe_{Th} site of ferrihydrite indicated that the As atom could spontaneously acquire electrons from the surface Fe_{Th} site. This result was also confirmed by the Bader charge analysis. The Bader charges for the Fe_{Th} and Fe_{Oh} atoms in the As−Fe complexes are shown in Table S7. The change of Bader charge (Δe_B) reflects the gain or loss of electrons and the transfer direction, which was defined as $\Delta e_B = e_{Bads} - e_B$, where e_B and e_{Bads} are the Bader charge of the Fe atom before and after As(V) adsorption on the mineral surface. After As(V) adsorption, the Δe_B of Fe_{Oh} in As−Fe_{Oh} complexes was altered slightly by −0.019 e. In contrast, there was a significant change of Δe_B to −0.136 e for the Fe_{Th} atom in As−Fe_{Th} complexes, which was 7.1 times higher than that for the Fe_{Oh} atom in As−Fe_{Oh} complexes. This result indicated that a significant redox reaction was taking place between As(V) and the Fe_{Th} sites. Importantly, the negative value of Δe_B for the Fe_{Th} atom indicated that the direction of electron transfer occurred from Fe_{Th} to the As atoms. This is the reason we observed the electron cloud gathering around the As atom after binding to the Fe_{Th} site of ferrihydrite. To sum up, structural Fe(II) in iron minerals reduces the charge resistance, thereby enabling electron transfer between the iron minerals and As(V).

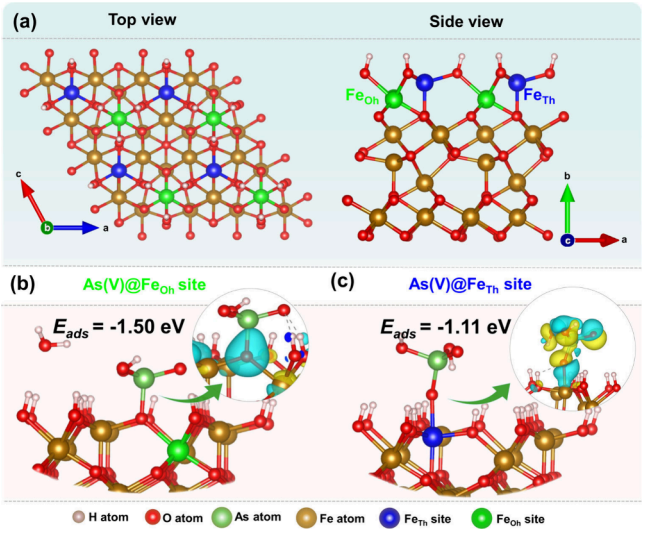

Figure 5. Top and side views of surface Fe_{Oh} (green color) and Fe_{Th} (blue color) sites on the optimized (001) ferrihydrite surface (a). The optimized structure and local electron density ($\Delta\rho$) of the $H_2AsO_4^{2-}$ ion adsorbed on the surface Fe_{Th} (b) and Fe_{Oh} (c) sites of (001) ferrihydrite, respectively. The chartreuse and cyan colors represent the charge accumulation and depletion, respectively.

3.6. Underlying Mechanism of As(V) Reduction on Ferrihydrite during Drying Process. According to the half-reaction equation $H_2AsO_4^- + 3H^+ + 2e^- \rightarrow HAsO_2 + 2H_2O$, two factors influence the reduction of As(V) to As(III). First, the availability of an electron donor is a prerequisite for this redox reaction. In this study, we utilized PAL analysis to confirm the abundance of oxygen vacancy clusters in poorly crystalline ferrihydrite, revealing the presence of nonstoichiometric oxygen content within its structure. The existence of oxygen vacancies influenced the Fe oxidation state, causing it to shift to a lower value to maintain electrostatic balance, thereby forming structural Fe(II) within the ferrihydrite. This observation aligned with previous work by Michel et al., who proposed a new chemical composition for ferrihydrite, highlighting a relatively low Fe oxidation state.[43] Additionally, we demonstrated that the structural Fe(II) within these iron minerals serves as a critical electron donor, driving the reduction of As(V) (Figures 4 and 5). Second, the pH of the reaction system significantly impacts the redox process. A

https://doi.org/10.1021/acs.est.4c10674
Environ. Sci. Technol. 2025, 59, 5191−5201

low pH condition increases the proton concentration, which accelerates the As redox reaction on the mineral surface. We observed that the reduction of As(V) adsorbed on ferrihydrite was significantly higher at lower pH (e.g., pH 5) compared to higher pH (e.g., pH 9) (Figure 1d). Interestingly, during the transition from wet to dry conditions, protons appear to concentrate in the mineral systems. For example, we measured the pH evolution of ferrihydrite minerals as the suspensions were concentrated through evaporation at room temperature. As shown in Table S8, the initial pH of the minerals decreased correspondingly as the solution volume was reduced. A similar phenomenon had been observed at the ice−water interface during freezing, where protons become highly concentrated in the grain boundary regions of ice.[53,54] Therefore, compared to the solution environment, the concentrated protons during the drying process provided a favorable condition to facilitate the half-reaction. Remarkably, water is a product of the above half-reaction. Therefore, according to Le Chatelier's principle, the drying process drives the half-reaction forward by removing water from the system. Based on our analyses, we propose that the reduction of As(V) on ferrihydrite under drought conditions can be attributed to structural Fe(II) acting as an electron donor, the drying-induced proton concentration effect, and the drying process promoting the forward reaction.

4. ENVIRONMENTAL SIGNIFICANCE

Soil arsenic pollution resulting from industrial and agricultural activities has garnered significant attention over the past decades, particularly in China.[55] Because the oxidation state of arsenic determines its mobility and toxicity in the environment, the transformation of As species, especially the formation of highly toxic and mobile As(III) species, warrants more attention than its total concentration. Although biotic and abiotic pathways for the reduction of As(V) to As(III) have been widely investigated in the past, these observations primarily took place in water-saturated aqueous systems, particularly in groundwater and sediments. The natural soil environment often has a relatively low moisture content, such as in paddy soil during drying periods and soil around industrial sites. Therefore, the soil environment is a typical nonsaturated aqueous system. Fe minerals are typical components of soil, which have a strong affinity toward arsenic, affecting the migration and fate of As. In this study, we observed for the first time the abiotic reduction of As(V) to As(III) by active iron minerals such as ferrihydrite and magnetite during the drying process. We provided both theoretical and experimental evidence to reveal the feasibility of electron transfer between the drought-sealed iron minerals and As(V). The findings of this study present a potentially important but so far overlooked abiotic pathway for As(V) reduction under dry soil conditions. Soil particles in the top layer are occasionally exposed to drought conditions, which could potentially mediate a significant abiotic reduction of As(V), in addition to biotic processes. Therefore, this new reduction pathway should be considered in the assessment of the fate of arsenic in soils.

■ ASSOCIATED CONTENT

Supporting Information

The Supporting Information is available free of charge at https://pubs.acs.org/doi/10.1021/acs.est.4c10674.

Details of preparation for hematite sample, characterization of PAL, four-point probe test, and Mössbauer measurements; As and Fe species analysis; fitting result of As 3d XPS and Fe 2p XPS; fitting parameters of Mössbauer spectra; calculation result of adsorption energies of As(V) on the ferrihydrite; the pH evolution of ferrihydrite minerals; and additional figures and tables as mentioned in this paper (PDF)

■ AUTHOR INFORMATION

Corresponding Author

Jingtao Hou − *State Environmental Protection Key Laboratory of Soil Health and Green Remediation, Hubei Key Laboratory of Soil Environment and Pollution Remediation, College of Resources and Environment, Huazhong Agricultural University, Wuhan 430070, China;* orcid.org/0000-0002-2472-8309; Email: houjt87@163.com

Authors

Yongjin Xiang − *State Environmental Protection Key Laboratory of Soil Health and Green Remediation, Hubei Key Laboratory of Soil Environment and Pollution Remediation, College of Resources and Environment, Huazhong Agricultural University, Wuhan 430070, China*

Lu Ren − *School of Civil Engineering, Suzhou University of Science and Technology, Suzhou 215009, China;* orcid.org/0000-0002-2166-1030

Juan Xiong − *State Environmental Protection Key Laboratory of Soil Health and Green Remediation, Hubei Key Laboratory of Soil Environment and Pollution Remediation, College of Resources and Environment, Huazhong Agricultural University, Wuhan 430070, China;* orcid.org/0000-0003-4414-536X

Biao Wan − *State Environmental Protection Key Laboratory of Soil Health and Green Remediation, Hubei Key Laboratory of Soil Environment and Pollution Remediation, College of Resources and Environment, Huazhong Agricultural University, Wuhan 430070, China;* orcid.org/0000-0003-2903-1655

Mingxia Wang − *State Environmental Protection Key Laboratory of Soil Health and Green Remediation, Hubei Key Laboratory of Soil Environment and Pollution Remediation, College of Resources and Environment, Huazhong Agricultural University, Wuhan 430070, China;* orcid.org/0000-0002-5244-432X

Wenfeng Tan − *State Environmental Protection Key Laboratory of Soil Health and Green Remediation, Hubei Key Laboratory of Soil Environment and Pollution Remediation, College of Resources and Environment, Huazhong Agricultural University, Wuhan 430070, China*

Andreas Kappler − *Geomicrobiology, Department of Geosciences, University of Tuebingen, Tuebingen 72076, Germany;* orcid.org/0000-0002-3558-9500

Complete contact information is available at: https://pubs.acs.org/10.1021/acs.est.4c10674

Notes

The authors declare no competing financial interest.

https://doi.org/10.1021/acs.est.4c10674
Environ. Sci. Technol. 2025, 59, 5191−5201

■ ACKNOWLEDGMENTS

This work was supported by the National Natural Science Foundation of China (42277015, 42277302, 41977022), the Natural Science Foundation of Hubei Province, China (2023AFD227), and the Key R&D Program of Hubei Province, China (2023BBB001). We thank Prof. Yuanzhi Li at Wuhan University of Technology for his help with DFT calculations and Dr. Jilin Bai at Center for Materials Research and Analysis (Wuhan University of Technology) for her help in XPS analysis. We also thank Beijing Synchrotron Radiation Facility (BSRF, China) at Beamline 1W1B and Hefei Synchrotron Radiation Light Source (HLS, China) at Beamline BL12B for XAS measurements.

■ REFERENCES

(1) Choong, T. S.Y.; Chuah, T.G.; Robiah, Y.; Gregory Koay, F.L.; Azni, I. Arsenic Toxicity, Health Hazards and Removal Techniques from Water: An Overview. *Desalination* **2007**, *217* (1−3), 139−166.
(2) Gorny, J.; Billon, G.; Lesven, L.; Dumoulin, D.; Madé, B.; Noiriel, C. Arsenic Behavior in River Sediments under Redox Gradient: A Review. *Sci. Total Environ.* **2015**, *505*, 423−434.
(3) Wang, J. N.; Zeng, X. C.; Zhu, X. B.; Chen, X. M.; Zeng, X.; Mu, Y.; Yang, Y.; Wang, Y. X. Sulfate Enhances the Dissimilatory Arsenate-Respiring Prokaryotes-Mediated Mobilization, Reduction and Release of Insoluble Arsenic and Iron from the Arsenic-Richs Ediments into Groundwater. *J. Hazard. Mater.* **2017**, *339*, 409−417.
(4) Cai, X. L.; Zhang, Z. N.; Yin, N. Y.; Du, H. L.; Li, Z. J.; Cui, Y. S. Comparison of Arsenate Reduction and Release by Three As(V)-Reducing Bacteria Isolated from Arsenic-Contaminated Soil of Inner Mongolia, China. *Chemosphere* **2016**, *161*, 200−207.
(5) Guo, H. M.; Liu, Z. Y.; Ding, S. S.; Hao, C. B.; Xiu, W.; Hou, W. G. Arsenate Reduction and Mobilization in the Presence of Indigenous Aerobic Bacteria Obtained from High Arsenic Aquifers of the Hetao Basin, Inner Mongolia. *Environ. Pollut.* **2015**, *203*, 50−59.
(6) Babechuk, M. G.; Weisener, C. G.; Fryer, B. J.; Paktunc, D.; Maunders, C. Microbial Reduction of Ferrous Arsenate: Biogeochemical Implications for Arsenic Mobilization. *Appl. Geochem.* **2009**, *24* (12), 2332−2341.
(7) Perez, J. P. H.; Tobler, D. J.; Thomas, A. N.; Freeman, H. M.; Dideriksen, K.; Radnik, J.; Benning, L. G. Adsorption and Reduction of Arsenate during the Fe(II)-Induced Transformation of Ferrihydrite. *ACS Earth Space Chem.* **2019**, *3* (6), 884−894.
(8) Jiang, J.; Bauer, I.; Paul, A.; Kappler, A. Arsenic Redox Changes by Microbially and Chemically Formed Semiquinone Radicals and Hydroquinones in a Humic Substance Model Quinone. *Environmen. Sci. Technol.* **2009**, *43* (10), 3639−3645.
(9) Troyer, L. D.; Tang, Y. Z.; Borch, T. Simultaneous Reduction of Arsenic(V) and Uranium(VI) by Mackinawite: Role of Uranyl Arsenate Precipitate Formation. *Environ. Sci. Technol.* **2014**, *48* (24), 14326−14334.
(10) Jin, X.; Wu, D. D.; Chen, Z. Y.; Wang, C.; Liu, C.; Gu, C. Surface Catalyzed Hydrolysis of Chloramphenicol by Montmorillonite under Limited Surface Moisture Conditions. *Sci. Total Environ.* **2021**, *770*, 144843.
(11) Jin, X.; Wu, D. D.; Ling, J. Y.; Wang, C.; Liu, C.; Gu, C. Hydrolysis of Chloramphenicol Catalyzed by Clay Minerals under Nonaqueous Conditions. *Environ. Sci. Technol.* **2019**, *53* (18), 10645−10653.
(12) Xu, S. H.; Lehmann, R. G.; Miller, J. R.; Chandra, G. Degradation of Polydimethylsiloxanes (Silicones) as Influenced by Clay Minerals. *Environ. Sci. Technol.* **1998**, *32* (9), 1199−1206.
(13) Liu, C.; Yu, H.-Y.; Liu, C.; Li, F.; Xu, X.; Wang, Q. Arsenic Availability in Rice from A Mining Area: is Amorphous Iron Oxide-Bound Arsenic A Source or Sink? *Environ. Pollut.* **2015**, *199*, 95−101.
(14) Cornell, R. M.; Schwertmann, U. In *The Iron Oxides: Structure, Properties, Reactions, Occurences and Uses*; Wiley-VCH, 2003.
(15) Liu, J.; Xiang, Y. J.; Chen, Y. W.; Zhang, H. J.; Ye, B. J.; Ren, L.; Tan, W. F.; Kappler, A.; Hou, J. T. Quantitative Contribution of Oxygen Vacancy Defects to Arsenate Immobilization on Hematite. *Environ. Sci. Technol.* **2023**, *57* (33), 12453−12464.
(16) Xiang, Y. J.; Liu, J.; Chen, Y. W.; Zhang, H. J.; Ren, L.; Ye, B. J.; Tan, W. F.; Andreas, K.; Hou, J. T. The Change of coordination Environments Induced by Vacancy Defects in Hematite Leads to a Contrasting Difference between Cation Pb(II) and Oxyanion As(V) Immobilization. *Environ. Pollut.* **2024**, *344*, 123318.
(17) Zhao, Z. W.; Meng, Y.; Yuan, Q. K.; Wang, Y. H.; Lin, L. M.; Liu, W. B.; Luan, F. B. Microbial Mobilization of Arsenic from Iron-Bearing Clay Mineral Through Iron, Arsenate, and Simultaneous Iron-Arsenate Reduction Pathways. *Sci. Total Environ.* **2021**, *763*, 144613.
(18) Sheng, A. X.; Liu, J.; Li, X. X.; Qafoku, O.; Collins, R. N.; Jones, A. M.; Pearce, C. I.; Wang, C.; Ni, J. R.; Lu, A. H.; Rosso, K. M. Labile Fe(III) from Sorbed Fe(II) Oxidation is the Key Intermediate in Fe(II)-Catalyzed Ferrihydrite Transformation. *Geochim. Cosmochim. Acta* **2020**, *272*, 105−120.
(19) Goncalves, P. R. G.; De Abreu, H. A.; Duarte, H. A. Arsenic Adsorption on Mn_3O_4 Surface: $As(OH)_3/AsO(OH)_3$ Oxidation Mechanism. *Appl. Surf. Sci.* **2022**, *580*, 152213.
(20) Yan, L.; Chan, T.; Jing, C. Arsenic Adsorption on Hematite Facets: Spectroscopy and DFT Study. *Environ. Sci.: Nano* **2020**, *7* (12), 3927−3939.
(21) Dzade, N. Y.; de Leeuw, N. H. Density Functional Theory Characterization of the Structures of H_3AsO_3 and H_3AsO_4 Adsorption Complexes on Ferrihydrite. *Environ. Sci-Proc. Imp.* **2018**, *20* (6), 977−987.
(22) Zheng, Q.; Tu, S. X.; Chen, Y. W.; Zhang, H. J.; Hartley, W.; Ye, B. J.; Ren, L.; Xiong, J.; Tan, W. F.; Kappler, A.; Hou, J. T. Micropore Sites In Ferrihydrite Are Responsible for Its Higher Affinity towards As(III) Relative to As(V). *Geochim. Cosmochim. Acta* **2023**, *348*, 27−40.
(23) Liu, C. H.; Chuang, Y. H.; Chen, T. Y.; Tian, Y.; Li, H.; Wang, M. K.; Zhang, W. Mechanism of Arsenic Adsorption on Magnetite Nanoparticles from Water: Thermodynamic and Spectroscopic Studies. *Environ. Sci. Technol.* **2015**, *49* (13), 7726−7734.
(24) Guo, Q.; Cao, Y.; Yin, Z.; Yu, Z.; Zhao, Q.; Shu, Z. Enhanced Removal of Arsenic from Water by Synthetic Nanocrystalline Iowaite. *Sci. Rep.* **2017**, *7*, 17546.
(25) Yang, T. Y.; Yu, D. Y.; Wang, D.; Yang, T.; Li, Z. X.; Wu, M. H.; Petru, M.; Crittenden, J. Accelerating Fe(III)/Fe(II) Cycle via Fe(II) Substitution for Enhancing Fenton-like Performance of Fe-MOFs. *Appl. Catal., B* **2021**, *286*, 119859.
(26) Chen, H.; Liu, Y. T.; Cai, T.; Dong, W. Y.; Tang, L.; Xia, X. N.; Wang, L. L.; Li, T. Boosting Photocatalytic Performance in Mixed-Valence MIL-53(Fe) by Changing Fe(II)/Fe(III) Ratio. *ACS. Appl. Mater. Inter.* **2019**, *11* (32), 28791−28800.
(27) Gao, C.; Su, Y.; Quan, X.; Sharma, V. K.; Chen, S.; Yu, H. T.; Zhang, Y. B.; Niu, J. F. Electronic Modulation of Iron-Bearing Heterogeneous Catalysts to Accelerate Fe(III)/Fe(II) Redox Cycle for Highly Efficient Fenton-like Catalysis. *Appl. Catal., B* **2020**, *276*, 119016.
(28) Gorski, C. A.; Scherer, M. M. Influence of Magnetite Stoichiometry on Fe(II) Uptake and Nitrobenzene Reduction. *Environ. Sci. Technol.* **2009**, *43* (10), 3675−3680.
(29) Doriguetto, A. C.; Fernandes, N. G.; Persiano, A. I. C.; Filho, E. N.; Greneche, J. M.; Fabris, J. D. Characterization of a Natural Magnetite. *Phys. Chem. Miner.* **2003**, *30* (5), 249−255.
(30) Rosso, K. M.; Yanina, S. V.; Gorski, C. A.; Larese-Casanova, P.; Scherer, M. M. Connecting Observations of Hematite (α-Fe_2O_3) Growth Catalyzed by Fe(II). *Environ. Sci. Technol.* **2010**, *44* (1), 61−67.
(31) Larese-Casanova, P.; Scherer, M. M. Fe(II) Sorption on Hematite: New Insights Based on Spectroscopic Measurements. *Environ. Sci. Technol.* **2007**, *41* (2), 471−477.
(32) Gorski, C. A.; Scherer, M. M. Determination of Nanoparticulate Magnetite Stoichiometry by Mossbauer Spectroscopy,

https://doi.org/10.1021/acs.est.4c10674
Environ. Sci. Technol. 2025, 59, 5191−5201

Acidic Dissolution, and powder X-Ray Diffraction: A Critical Review. *Am. Mineral.* **2010**, *95* (7), 1017−1026.
(33) Zhang, G. Q.; Yuan, Z. D.; Lei, L.; Lin, J. R.; Wang, X.; Wang, S. F.; Jia, Y. F. Arsenic Redistribution and Transformation during Fe(II)-Catalyzed Recrystallization of As-Adsorbed Ferrihydrite under Anaerobic Conditions. *Chem. Geo.* **2019**, *525*, 380−389.
(34) Das, S.; Hendry, M. J.; Essilfie-Dughan, J. Effects of Adsorbed Arsenate on the Rate of Transformation of 2-Line Ferrihydrite at pH 10. *Environ. Sci. Technol.* **2011**, *45* (13), 5557−5563.
(35) Das, S.; Hendry, M. J.; Essilfie-Dughan, J. Transformation of Two-Line Ferrihydrite to Goethite and Hematite as a Function of pH and Temperature. *Environ. Sci. Technol.* **2011**, *45* (1), 268−275.
(36) Joharipannalal, S.; Crowe, S. A.; Cioppa, M. T.; Symons, D. T. A.; Sturm, A.; Fowle, D. A. Room-Temperature Magnetic Properties of Ferrihydrite: A Potential Magnetic Remanence Carrier? *Earth Planet Sci. Lett.* **2005**, *236* (3−4), 856−870.
(37) Seehra, M. S.; Babu, V. S.; Manivannan, A.; Lynn, J. W. Neutron Scattering and Magnetic Studies of Ferrihydrite Nanoparticles. *Phys. Rev. B* **2000**, *61* (5), 3513−3518.
(38) Hiemstra, T. Surface and Mineral Structure of Ferrihydrite. *Geochim. Cosmochim. Acta* **2013**, *105*, 316−325.
(39) Filip, J.; Zboril, R.; Schneeweiss, O.; Zeman, J.; Cernik, M.; Kvapil, P.; Otyepka, M. Environmental Applications of Chemically Pure Natural Ferrihydrite. *Environ. Sci. Technol.* **2007**, *41* (12), 4367−4374.
(40) Michel, F. M.; Ehm, L.; Liu, G.; Han, W. Q.; Antao, S. M.; Chupas, P. J.; Lee, P. L.; Knorr, K.; Eulert, H.; Kim, J.; Grey, C. P.; Celestian, A. J.; Gillow, J.; Schoonen, M. A. A.; Strongin, D. R.; Parise, J. B. Similarities in 2-and 6-Line Ferrihydrite Based on Pair Distribution Function Analysis of X-ray Total Scattering. *Chem. Mater.* **2007**, *19* (6), 1489−1496.
(41) Elhilo, M.; O'Grady, K.; Chantrell, R. W. The Ordering Temperature in Fine Particle-Systems. *J. Magn. Magn. Mater.* **1992**, *117* (1−2), 21−28.
(42) Wang, X. M.; Zhu, M. Q.; Koopal, L. K.; Li, W.; Xu, W. Q.; Liu, F.; Zhang, J.; Liu, Q. S.; Feng, X. H.; Sparks, D. L. Effects of Crystallite Size on the Structure and Magnetism of Ferrihydrite. *Environ. Sci.:Nano* **2016**, *3* (1), 190−202.
(43) Michel, F. M.; Barrón, V.; Torrent, J.; Morales, M. P.; Serna, C. J.; Boily, J. F.; Liu, Q. S.; Ambrosini, A.; Cismasu, A. C.; Brown, G. Ordered Ferrimagnetic Form of Ferrihydrite Reveals Links among Structure, Composition, and Magnetism. *Proc. Natl. Acad. Sci. U. S. A.* **2010**, *107* (7), 2787−2792.
(44) Notini, L.; Latta, D. E.; Neumann, A.; Pearce, C. I.; Sassi, M.; N'Diaye, A. T.; Rosso, K. M.; Scherer, M. M. The Role of Defects in Fe(II)-Goethite Electron Transfer. *Environ. Sci. Technol.* **2018**, *52* (5), 2751−2759.
(45) Han, X. H.; Tomaszewski, E. J.; Sorwat, J.; Pan, Y. X.; Kappler, A.; Byrne, J. M. Effect of Microbial Biomass and Humic Acids on Abiotic and Biotic Magnetite Formation. *Environ. Sci. Technol.* **2020**, *54* (7), 4121−4130.
(46) Dutta, S.; Chattopadhyay, S.; Jana, D.; Banerjee, A.; Manik, S.; Pradhan, S. K.; Sutradhar, M.; Sarkar, A. Annealing Effect on Nano-ZnO Powder Studied from Positron Lifetime and Optical Absorption Spectroscopy. *J. Appl. Phys.* **2006**, *100* (11), 114328.
(47) Liu, X. W.; Zhou, K. B.; Wang, L.; Wang, B. Y.; Li, Y. D. Oxygen Vacancy Clusters Promoting Reducibility and Activity of Ceria Nanorods. *J. Am. Chem. Soc.* **2009**, *131* (9), 3140−3141.
(48) Kong, M.; Li, Y.; Chen, X.; Tian, T.; Fang, P.; Zheng, F.; Zhao, X. Tuning the Relative Concentration Ratio of Bulk Defects to Surface Defects in TiO_2 Nanocrystals Leads to High Photocatalytic Efficiency. *J. Am. Chem. Soc.* **2011**, *133* (41), 16414−16417.
(49) Chakrabarti, S.; Chaudhuri, S.; Nambissan, P. M. G. Positron Annihilation Lifetime Changes Across the Structural Phase Transition in Nanocrystalline Fe_2O_3. *Phys. Rev. B* **2005**, *71* (6), 064105.
(50) Wasinger, E. C.; de Groot, F. M. F.; Hedman, B.; Hodgson, K. O.; Solomon, E. I. L-edge X-Ray Absorption Spectroscopy of Non-Heme Iron Sites: Experimental Determination of Differential Orbital Covalency. *J. Am. Chem. Soc.* **2003**, *125* (42), 12894−12906.
(51) Baker, M. L.; Mara, M. W.; Yan, J. J.; Hodgson, K. O.; Hedman, B.; Solomon, E. I. K- and L-edge X-Ray Absorption Spectroscopy (XAS) and Resonant Inelastic X-Ray Scattering (RIXS) Determination of Differential Orbital Covalency (DOC) of Transition Metal Sites. *Coordin. Chem. Rev.* **2017**, *345*, 182−208.
(52) Hua, W. J.; Tian, G. J.; Fronzoni, G.; Li, X.; Stener, M.; Luo, Y. Fe L-Edge X-Ray Absorption Spectra of Fe(II) Polypyridyl Spin Crossover Complexes from Time-Dependent Density Functional Theory. *J. Phys. Chem. A* **2013**, *117* (51), 14075−14085.
(53) Heger, D.; Klánová, J.; Klán, P. Enhanced Protonation of Cresol Red in Acidic Aqueous Solutions Caused by Freezing. *J. Phys. Chem. B* **2006**, *110* (3), 1277−1287.
(54) Min, D. W.; Choi, W. Accelerated Reduction of Bromate in Frozen Solution. *Environ. Sci. Technol.* **2017**, *51* (15), 8368−8375.
(55) Zhang, S. Y.; Zhang, J. J.; Niu, L. L.; Chen, Q.; Zhou, Q.; Xiao, N.; Man, J.; Ma, J. Q.; Wei, C. L.; Zhang, S. H.; Luo, Y. M.; Yao, Y. J. Escalating Arsenic Contamination Throughout Chinese Soils. *Nat. Sustain.* **2024**, *7* (6), 766−775.

https://doi.org/10.1021/acs.est.4c10674
Environ. Sci. Technol. 2025, 59, 5191−5201